Development of the Chemical Imaging Sensor – Image Correction and Flow System –

Tatsuo Yoshinobu

Professor
Department of Biomedical Engineering, Graduate School of Biomedical Engineering
E-mail: nov@ecei.tohoku.ac.jp

1. Introduction

Our laboratory is engaged in the development of the chemical imaging sensor [1-6], a semiconductor-based chemical sensor that can visualize the two-dimensional distribution of ion concentration in the specimen. The chemical imaging sensor is based on the principle of the light-addressable potentiometric sensor (LAPS) [7]. In the chemical imaging sensor, the distribution of carriers in the semiconductor layer reflects the distribution of ion concentration on the sensing surface, which is read out in the form of photocurrent signal.

Chemical sensors based on semiconductor devices are advantageous for miniaturization, integration with the peripheral circuits and fabrication of various structures on their surfaces with the help of microfabrication techniques such as photolithography. A well-known semiconductor-based chemical sensor is the ion-sensitive field-effect transistor (ISFET) [8,9], which has the field-effect structure or the electrolyte-insulator-semiconductor (EIS) structure. The ISFET is put to practical use, for example, in a portable pH meter. The EIS capacitive sensor and the light-addressable potentiometric sensor (LAPS) are other examples of chemical sensors based on the same EIS structure [10,11]. Figure 1 schematically compares the structures of these three field-effect-based chemical sensors.
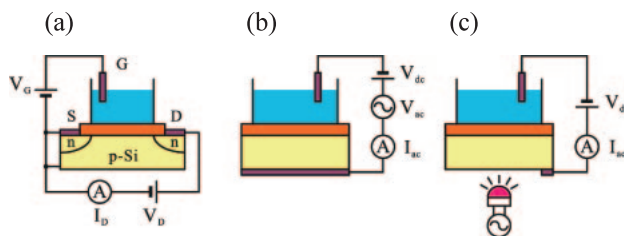

Fig. 1. Structures of (a) ISFET, (b) EIS capacitive sensor and (c) LAPS.

Chemical sensors based on the EIS structure detect the change of the distribution of carriers in the semiconductor layer through the field effect, which responds to the change of the ion concentration of the solution in contact with the sensing surface of the insulating layer. The ISFET detects the change of the conductance of the channel between the source and the drain electrodes, whereas the EIS capacitive sensor and the LAPS detect the change of the capacitance of the depletion layer at the semiconductor-insulator interface. In the case of a p-type semiconductor, the depletion layer grows thicker and the capacitance of the depletion layer becomes smaller when the sensing surface is more positively charged.

In the LAPS measurement, a photocurrent is generated to detect the change of the capacitance of the depletion layer. The back surface of the sensor plate is illuminated with a light beam modulated at a frequency of several kHz, and the amplitude of the ac photocurrent is measured as a function of the bias voltage applied to the EIS system.

Figure 2 shows typical current-voltage characteristics of a pH-sensitive LAPS with a Ta_2O_5 film as the insulating layer. A positive bias (applied to the solution with respect to the semiconductor substrate) in Fig.2 corresponds to the depletion and inversion states of the semiconductor layer, and a negative bias corresponds to the accumulation state. Due to the pH sensitivity of the Ta_2O_5 surface, the current – voltage ($I - V$) curve shifts along the voltage axis with a nearly Nernst value of pH sensitivity, 57.9 mV/pH.
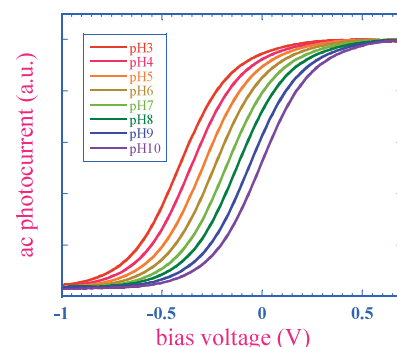

Fig. 2. Current-voltage characteristics of LAPS.

The measuring area of a LAPS sensor is restricted to the illuminated area, and therefore, many measuring spots can be defined on the sensing surface of a single sensor plate. One of the applications based on this feature is a multisensor [12,13], in which a plurality of ion-sensitive membranes are integrated on the sensing surface for the detection of various ions. Each of the ion-sensitive membranes on the sensing surface can be independently accessed by a probe light, which generates a photocurrent with an amplitude being dependent on the concentration of a specific ion. In this way, a single sensor plate can be used for the measurement of various ions.

Chemical imaging is another application which takes advantage of the addressability of LAPS. When the ion concentration is spatially distributed in the solution in contact with the sensing surface, the width and the capacitance of the depletion layer in the semiconductor layer is correspondingly distributed as shown in Fig. 3. By using a focused laser beam that scans the semiconductor substrate two-dimensionally and recording the photocurrent at each pixel on the sensing surface, a chemical image of the ion concentration is obtained.
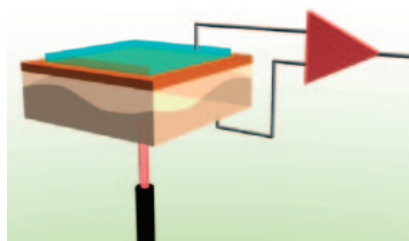

Fig. 3. Principle of the chemical imaging sensor. The photocurrent is dependent on the width of the depletion layer, which is distributed in response to the spatial distribution of the ion concentration on the sensing surface.

In this study, an image correction method was developed to remove artifacts in the chemical images, which have been a major problem. Two types of artifacts due to the non-uniformities of sensor plates were distinguished and removed by the developed method [14].

A measurement system with a flow channel on the sensing surface was fabricated for the reduction of analyte solution. As an example of biosensor application of this system, a flow measurement system with an enzyme reaction chamber was constructed. The reaction time in the enzyme reaction chamber was controlled with the flow rate, and the product of the enzymatic reaction was detected in the downstream.

2. Image Correction
2.1. Non-uniformities of sensor plates

The chemical imaging sensor relies on the variation of the photocurrent in response to the ion concentration at the illuminated position. While a focused laser beam scans the sensor plate under a fixed bias voltage, the amplitude of the ac photocurrent is recorded at each pixel. The obtained photocurrent map can be converted into a potential map by using the slope of the $I - V$ curve, and then further converted into an ion concentration map by using the slope sensitivity (variation of potential per decade of ion concentration) of the sensing surface.

Figure 4 shows an example of a photocurrent map of a homogeneous buffer solution of pH 7 obtained by the chemical imaging sensor. Since there is no distribution of ion concentration in the buffer solution, a uniform map should be obtained for an ideal sensor plate. In reality, however, stripe shadows, spots and a scratch are observed in Fig. 4. These features are artifacts due to the non-uniformities of the sensor plate. The photocurrent map in Fig. 4 can be converted into a pH map by using the slope of the $I - V$ curve, 0.69 μA/V and the slope sensitivity of the sensing surface, 57.9 mV/pH in this case. In this example, 0.1 μA of variation in photocurrent results in a very large variation of about 2.5 on the pH scale, which would be unacceptable for most applications. Therefore, development of an image correction method to remove these artifacts is essential for the practical application of the chemical imaging sensor.
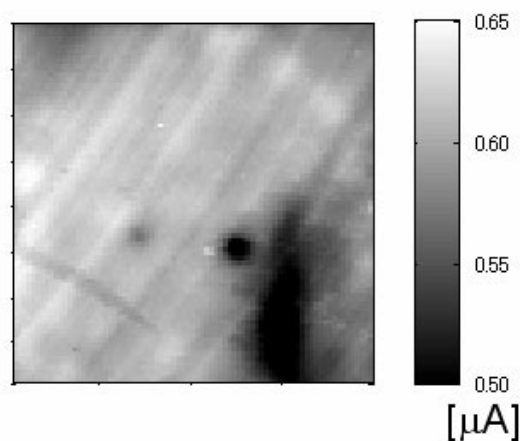

Fig. 4. An example of a chemical image with artifacts obtained by the chemical imaging sensor. Stripe shadows, spots and a scratch were observed in the image, even though the solution in contact with the sensing surface was homogeneous.

2.2. Origins of artifacts

Among the artifacts observed in Fig. 4, the stripe patterns are known to be an artifact due to the striation defects in the silicon substrate [15,16].

In the chemical imaging sensor, the back surface of the silicon substrate is illuminated with the probe light, which is absorbed in silicon and generates photocarriers. Out of the generated photocarriers, only those that arrive at the band bending near the insulator − semiconductor interface without recombination contribute to the photocurrent signal. The recombination probability of minority carriers reflects the spatial distribution of crystal defects in the silicon substrate. Under this situation, the height of the $I − V$ curve varies with the position on the sensing surface as shown in Fig. 5.

The striation defects already exist in the as-grown silicon ingot and distribute as concentric circles. Their spatial distribution in a sensor plate is determined when it is cut out from a silicon wafer, and will not change with the repeated use of the sensor plate.
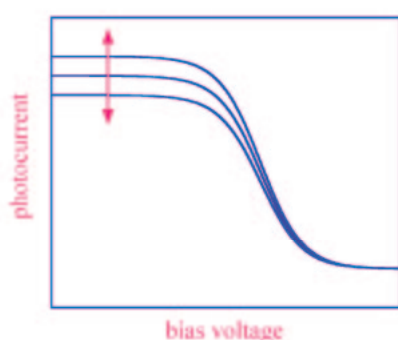

Fig. 5. Variation of photocurrent due to the distribution of the lifetime of minority carriers in the semiconductor substrate.

In addition to the distribution of photocurrent due to defects, there is also a spatial distribution of the so-called flat-band potential of the EIS system in the sensor plate. Variation of the flat-band potential results in a shift of the $I − V$ curve along the voltage axis as shown in Fig. 6. Since the chemical imaging sensor measures the photocurrent map at a fixed bias voltage, a local shift of the $I − V$ curve results in variation of photocurrent measured at each location. The spatial distribution of the flat-band potential is expected to change with the repeated use of the sensor plate due to contamination of the sensing surface or incorporation of ions into the insulating layer. The sensor plate used for the measurement of the photocurrent map in Fig. 4 had been used for the measurement of ions generated by electrolysis with a pair of electrodes, one of which had been placed in the proximity of the sensing surface. The dark region observed at the lower right corner of Fig. 4 is a result of this history of the sensor plate.

As described above, the chemical images obtained by the chemical imaging sensor include two types of artifacts due to the non-uniformities of the sensor plate. Those two artifacts have different physical origins and results in variation of the height of the $I − V$ curve and a shift of the $I − V$ curve, respectively.
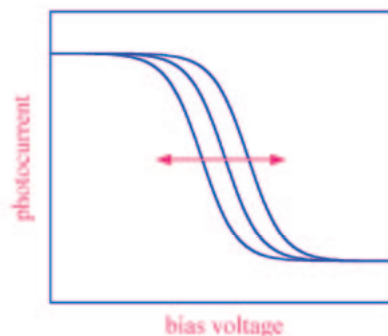

Fig. 6. Shift of the $I − V$ curve along the voltage axis due to the distribution of the flat-band potential.

The image correction method developed in this study separates the two types of artifacts and generates a pair of calibration maps for individual sensor plate, i.e., a photocurrent distribution map and a potential distribution map. Once a set of calibration maps are prepared for a sensor plate, the chemical images obtained with the same sensor plate can be corrected with these maps as far as the non-uniformities of the sensor plate remain the same.

2.3. Procedures of image correction
2.3.1. Current distribution map

To remove the first type of artifacts, i.e., the distribution of photocurrent due to defects in the semiconductor substrate, it is necessary to obtain a current distribution map of the particular sensor plate. In the saturation region of the $I − V$ curve shown in Fig. 6, where the EIS system is in the inversion state, the width of the depletion layer and its capacitance are no more dependent on the bias voltage applied to the EIS system. A photocurrent image measured in this region for a homogeneous solution in contact with the sensing surface can be used as a calibration map to remove the artifacts. A better quality of current distribution map is obtained by averaging a plurality of such maps.
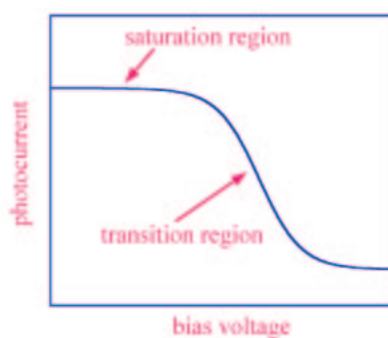

Fig. 7. Explanation of the saturation region and the transition region of the $I − V$ curve.

Figure 8 is an example of a current distribution map obtained by averaging 5 photocurrent images measured for a homogeneous buffer solution of pH 7 at a bias voltage of -1.5 V in the saturation region. In this map, stripe patterns corresponding to the distribution of striation defects in the silicon substrate are observed. The density scale on the right side shows the amplitude of the photocurrent normalized to the average value in the sensing area. In the dark regions of this map, the photocurrent is relatively smaller due to higher recombination rate of minority carriers at defects.
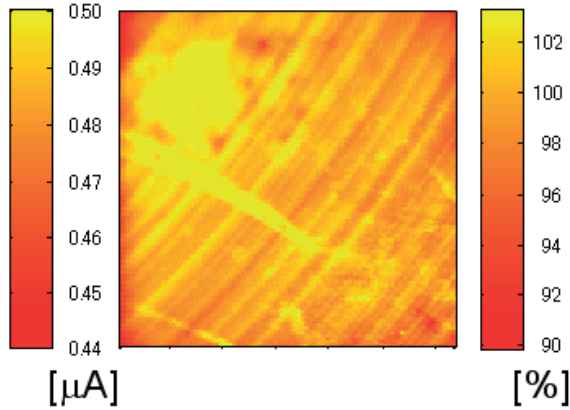

Fig. 8. Current distribution map generated from 5 photocurrent images of a homogeneous pH 7 buffer solution measured at a bias voltage of -1.5 V in the saturation region.

2.3.2. Potential distribution map

To remove the second type of artifacts, i.e., the distribution of the flat-band potential, it is necessary to obtain a potential distribution map of the particular sensor plate, which shows the distribution of the shift of the $I - V$ curve along the voltage axis at each position on the sensing surface For this purpose, photocurrent images for a homogeneous solution are measured at several bias voltages in the transition region of Fig.7. It should be noted that these photocurrent images are not free from the first type of artifacts, which are removed by dividing each photocurrent image with the current distribution map in Fig.8.

Next, the photocurrent value at each pixel in the corrected photocurrent image is converted into potential, or the shift of the $I - V$ curve along the voltage axis. Let $I(i, x, y)$ be the photocurrent at pixel (x, y) in the i th image, $I(i)$ be the average value in the sensing area, then the corresponding potential at pixel (x, y) in the i th image is given by

$$\phi(i, x, y) = \frac{I(i, x, y) - I(i)}{-S_{ave}} \qquad (1)$$

with respect to the average potential in the sensing area,

where S_{ave} (< 0) is the average slope of the $I - V$ curve at the middle of the transition region in Fig.7. The potential distribution map obtained in this way shows the distribution of the flat-band potential of the particular sensor plate. A better quality of potential distribution map can be obtained by averaging a plurality of such maps.

Figure 9 shows an example of a potential distribution map synthesized from 25 photocurrent images measured for a homogeneous buffer solution of pH 7 at 5 different bias voltages of -1.13, -1.12, -1.11, -1.10, and -1.09 V. The density scale on the right side shows the local potential shift with respect to the average.

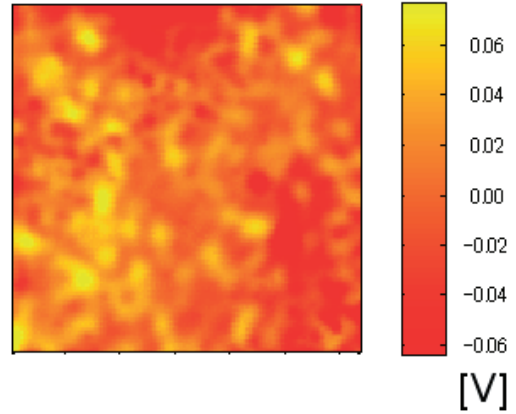Fig. 9. Potential distribution map generated from 25 photocurrent images of a homogeneous pH 7 buffer solution measured at bias voltages of -1.13, -1.12, ..., and -1.09 V in the transition region.

As described above, a set of calibration maps, i.e., a current distribution map (Fig.8) and a potential distribution map (Fig.9) are calculated from a series of photocurrent images measured for a homogeneous solution at various bias voltages in the saturation and transition regions of the $I - V$ curve.

After a homogeneous solution for calibration is brought into contact with the sensing surface, the rest of the above procedures, i.e., acquisition of a series of photocurrent images at different bias voltages and generation of two calibration maps can be automatically carried out by a control software.

2.3.3. Conversion and correction of images

A photocurrent image acquired by the chemical imaging sensor is converted into a potential image using the average slope of the transition region, and further converted into an ion concentration image using the slope sensitivity of the sensor plate.

The potential at each pixel can be defined as the bias voltage in the transition region at which the photocurrent is half the maximum in the saturation region. According to this definition, the photocurrent $I(x, y)$ at pixel (x, y) is converted into the potential $V(x, y)$ by

138

$$V(x, y) = V_\mathrm{B} + \frac{I(x, y) - I_\mathrm{S}/2}{-S}, \qquad (2)$$

where V_B is the bias voltage at which the photocurrent image is acquired, I_S is the maximal photocurrent in the saturation region, S is the average slope of the $I - V$ curve at the middle of the transition region.
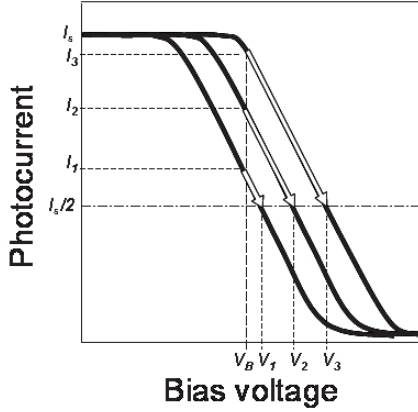

Fig. 10. Conversion of the distribution of photocurrent into the distribution of flat-band potential.

Once a set of calibration maps are prepared for a sensor plate, chemical images acquired with the same sensor plate can be corrected by the following steps.

(1) The acquired photocurrent image is divided with the current distribution map to remove the first type of artifacts.
(2) The photocurrent image is converted into a potential image according to eq.2.
(3) The potential distribution map is subtracted from the potential image to remove the second type of artifacts.

2.4. Performance of image correction

Figure 11 shows an example of image correction applied to a chemical image.

Figure 11(a) is a photocurrent image of a homogeneous KCl solution measured by the chemical imaging sensor. The scale on the left side shows the photocurrent, and the scale on the right side shows the potential calculated by conversion according to eq.2. In this image, both types of artifacts, i.e., the current distribution due to defects and the potential distribution due to the flat-band shift are observed. Thin lines in Fig.11(c) shows the histogram of the potential value at each pixel in Fig.11(a), which is broadly distributed with a standard deviation of 34.1 mV or 0.58 on the pH scale. A smaller variation of pH in the sample is hidden by artifacts and cannot be visualized with this sensor plate unless these artifacts are removed.

Figure 11(b) shows the potential image after applying the image correction procedures. Artifacts are almost removed and much more homogeneous image is obtained. The thick lines in Fig. 11(c) shows the histogram of the potential value at each pixel in Fig. 11(b), which shows a narrower distribution with a standard deviation of 5.3 mV (or 0.09 on the pH scale). By comparing the values of standard deviation, it is concluded that 85% of artifacts were removed by the image correction procedures developed in this study. It is expected that fine structures hidden by artifacts in a pH image are revealed by this image correction.

A closer look at Fig. 11(b) reveals, however, that artifacts are not completely removed. Followings are the possible reasons for the residual artifacts.
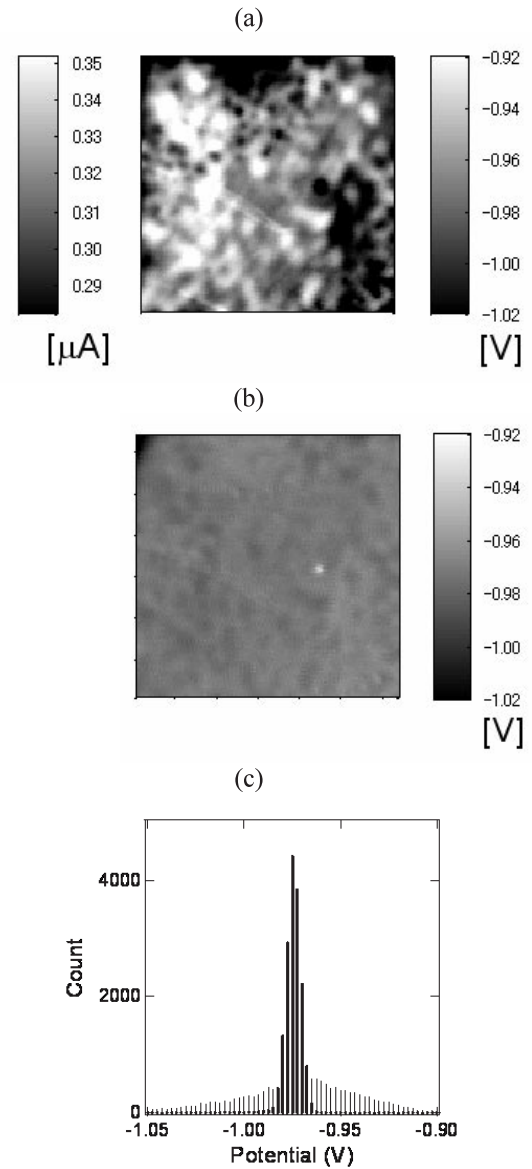

Fig. 11. Chemical images of a homogeneous KCl solution (a) before and (b) after image correction. (c) Histogram of potential distribution in chemical images before (thin lines) and after (thick lines) image correction.

(1) It was assumed that the photocurrent was constant in the saturation region. In reality, however, there is a slight dependence of the photocurrent on the bias voltage. The current distribution map generated from a photocurrent image at a fixed bias voltage in this situation is affected by the distribution of the flat-band potential.

(2) The $I - V$ curve was approximated with a straight line in the transition region. In reality, however, the $I - V$ curve is S-shaped, and therefore, the current-to-potential conversion by linear approximation results in a certain error.

These problems may be solved by parameterization of $I - V$ curves with two parameters, i.e., the height along the current axis and the shift along the voltage axis. By fitting the photocurrent values measured at various bias voltages by a parameterized curve, these two parameters can be simultaneously determined for each pixel.

3. Flow System
3.1. Advantage of flow system

In a microfluidic device such as a Lab-on-a-Chip and a μTAS, reactions and diagnoses are completed while the analyte solution flows through microfabricated channels. The advantages of microfluidic devices include miniaturization of the measurement system, reduction of reagents and easy handling of disposable chips.

Fluorescent labels are frequently used for high-sensitive detection of chemical species in a microfluidic device. For label-free measurements, microelectrodes and electrochemical sensors can be embedded in the microchannel.

Since the chemical imaging sensor is capable of measuring analyte at arbitrary positions on the sensing surface, it can serve as a platform for building microfluidic devices with multiple measuring sites. An arbitrary shape of microchannels can be formed on the flat surface of the chemical imaging sensor as shown in Fig. 12, and the concentration of analyte can be measured at an arbitrary point within the microchannel. By using the principle of frequency division multiplex [17,18], in which a plurality of light sources illuminate different points with different frequencies, the concentrations of chemical species can be simultaneously monitored at a plurality of positions.
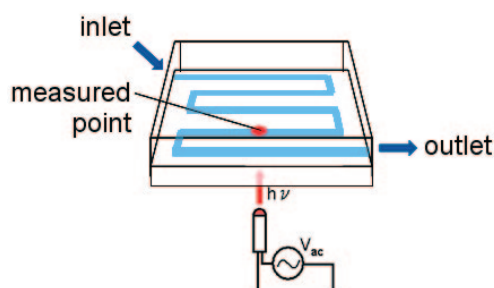

Fig. 12. Application of the chemical imaging sensor to measurement of ions in a flow channel.

3.2. Enzyme reaction chamber

In this study, the chemical imaging sensor was combined with a flow channel and an enzyme reaction chamber. Figure 13(a) and (b) show the schematic and assembly of the measurement cell with an externally attached enzyme reaction chamber. The measurement cell is made of plexiglass and the enzyme reaction chamber is a U-shaped silicone tube with an internal diameter of 1 mm. The enzyme reaction chamber has an inner volume of 33 μL and accommodates glass beads, on which enzyme molecules are immobilized. Two linear channels (W. 1 mm, H. 1.8 mm, L. 9 mm) lie on the sensing surface in the upstream and downstream of the enzyme reaction chamber for differential measurement, and the middle of each channel can be illuminated with a laser beam emitted from an optical fiber.
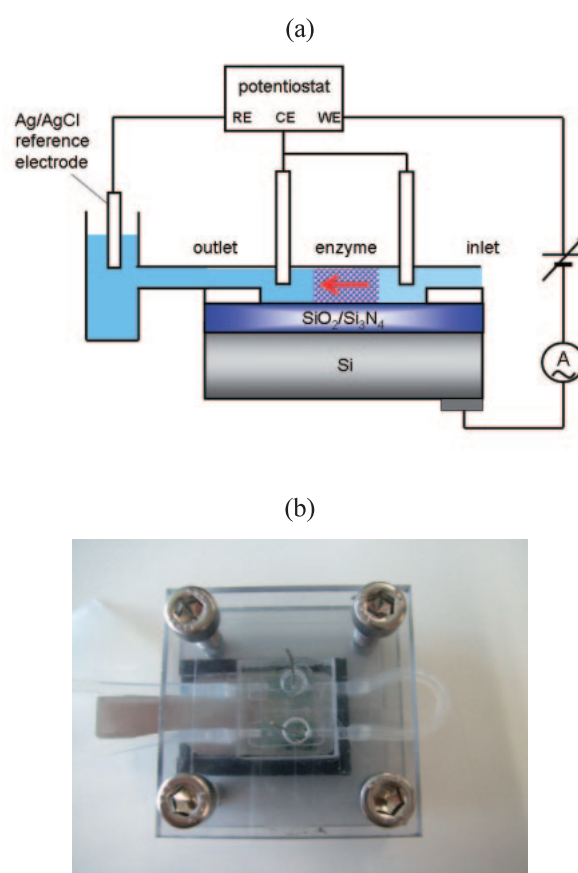
(a)

(b)

Fig. 13. (a) Configuration of the chemical imaging sensor combined with a flow channel and an enzyme reaction chamber. (b) A prototype system with a U-shaped enzyme reaction chamber attached to two flow channels on the sensing surface.

3.3. Immobilization of enzyme on glass beads

A urea sensor based on the enzymatic reaction of urease was fabricated. Urease catalyzes the following reaction of hydrolysis and produces ammonia. The concentration of urea can be determined by detecting the rise of pH value.

$$CO(NH_2)_2 + H_2O \rightarrow CO_2 + 2NH_3$$
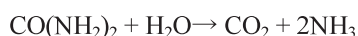
The enzyme reaction chamber was loaded with glass beads (200 μm in diameter), on which urease was immobilized with the following procedure.

(1) Glass beads are sonicated in ethanol and then dried in an oven at 100°C.
(2) Glass beads are immersed in dehydrated methanol with 10% aminopropyltriethoxysilane (APTES) for one hour to silanize the surface.
(3) Glass beads are immersed in 20% glutaraldehyde for one hour to introduce aldehyde groups.
(4) Glass beads are immersed in 10 unit/ml solution of urease overnight to immobilize enzyme molecules on the surface.

Before measuring urea with the developed sensor, the efficiency of enzymatic reaction catalyzed by urease molecules on the glass beads was estimated as follows. After immobilization of urease, 250 mg of glass beads were put into a solution with a known concentration of urea for enzymatic reaction, and then, after every 5 minutes, the solution was sampled for determination of produced ammonia by the indophenol blue absorptiometry.

Figure 14 shows the increase of ammonia concentration as a function of time. The rate of ammonia production catalyzed by urease on glass beads (calculated as the slope of S3) was 0.322 μmol/min. The urease solution before immersion of glass beads catalyzed ammonia production at a rate of 2.37 μmol/min (slope of S1), and the mixture of the residual urease after immersion of glass beads and the wash solution after rinsing glass beads catalyzed the reaction at a rate of 1.13 μmol/min (slope of S2). Therefore, the overall efficiency of the enzymatic activity of urease molecules immobilized on glass beads is estimated to be
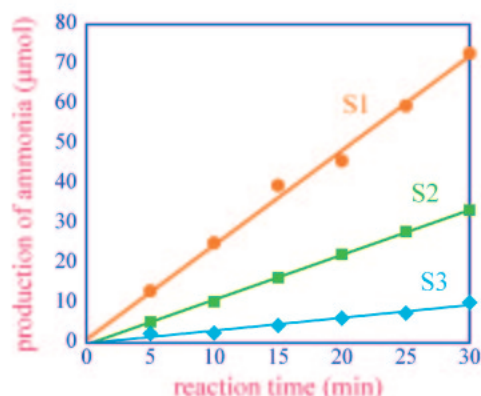

Fig. 14. Production of ammonia by hydrolysis of urea catalyzed by (S1) urease in the solution before immersion of glass beads, (S2) residual urease in the solution after immersion of glass beads and urease in the wash solution after rinsing glass beads, and (S3) urease immobilized on glass beads.

$$\frac{0.322}{2.37 - 1.13} = 26\%$$

of those in the solution.

Assuming the activity of urease as written on the specification sheet, the rate of reaction catalyzed by one monolayer of urease molecules (assumed to have a spherical shape and a diameter of 10 nm) immobilized on 250 mg of glass beads (with a diameter of 200 μm) is calculated to be 0.422 μmol/min.

3.4. Measurement in flow system

The pH change in the course of hydrolysis of urea was detected with the prototype system. The external view of the measurement system is shown in Fig. 15.
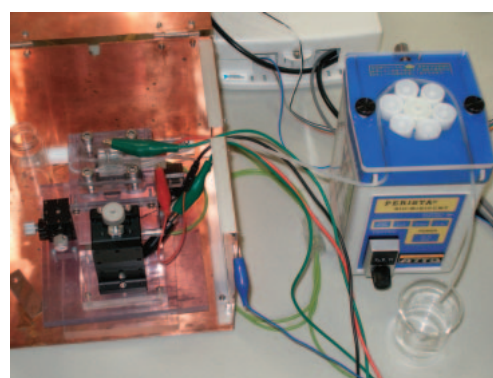

Fig. 15. LAPS measurement setup with a flow system.

The measurement cell with an enzyme reaction chamber shown in Fig. 13(b) was placed in the shield box. The middle of the flow channel in the downstream of the enzyme reaction chamber was illuminated with a laser beam guided with an optical fiber. The measurement was carried out in the constant-current mode [19], in which the bias voltage applied to the sensor is feedback-controlled to maintain the output photocurrent signal at a fixed value. In this mode, the temporal change of pH is recorded as variation of the applied bias voltage as a function of time.

The enzyme reaction chamber was loaded with glass beads, on which urease molecules were immobilized. The weight and the volume of loaded glass beads were 20 mg and 8 μL, respectively. The reaction volume is defined as the unoccupied volume of the chamber, $33 - 8 = 25$ μL. The solution to be measured was supplied with a Perista pump from outside of the shield box. The reaction time is calculated by dividing the reaction volume of the chamber (25 μL) with the flow rate (μL/min).

According to the results of preliminary experiments, the urea concentration above 10^{-1} mol/L and below 10^{-2} mol/L in this system corresponded to excess of substrate and enzyme, respectively. Under the condition of excess enzyme, the initial rate of

reaction is proportional to the concentration of the substrate, and therefore, the production of ammonia is proportional to the product of the reaction time and the concentration of the substrate.

The variation of sensor signal was measured in response to a change of the flow rate (and the reaction time) of 10^{-1} mol/L urea with 1 mM PBS solution under the condition of excess substrate. Figure 16 shows the variation of the potential observed at the measuring point in the downstream of the enzyme reaction chamber in response to the abrupt change of the flow rate from 250 µL/min (reaction time = 6 sec) to 150 µL/min (reaction time = 10sec). A variation of about 5 mV (or about 0.1 on the pH scale) was recorded.
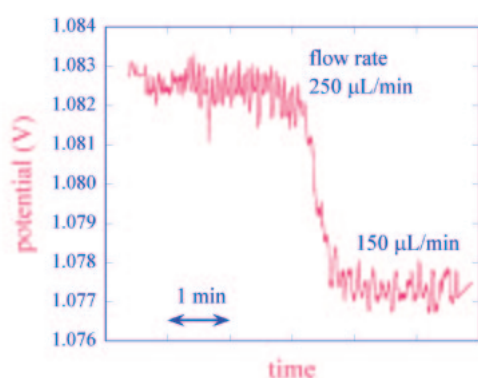

Fig. 16. Transient change of the potential recorded in the downstream of the reaction chamber in response to the change of the flow rate of urea solution.

In Fig. 17, the flow rate was successively changed to various values between 7.5 and 250 µL/min. By measuring the difference of the output potentials for two flow rates, the drift on the potential scale can be partially cancelled.
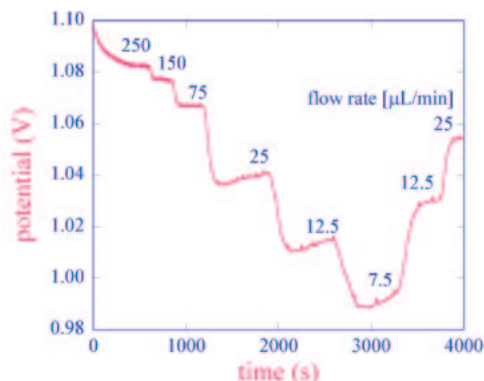

Fig. 17. Change of the potential recorded in the downstream of the reaction chamber for various flow rates of urea solution.

Next, the dependence of the sensor signal on the urea concentration was measured under the condition of excess enzyme. The concentration of urea was changed in the range of 3×10^{-4} to 3×10^{-2} mol/L, and the flow rate was abruptly changed from 100 µL/min (reaction time = 15 sec) to 12.5 µL/min (reaction time = 120 sec). In Fig.18, the variation of potential observed in the downstream of the enzyme reaction chamber in response to the abrupt change of the flow rate is plotted versus the logarithm of the urea concentration. The potential shift increased with the urea concentration.
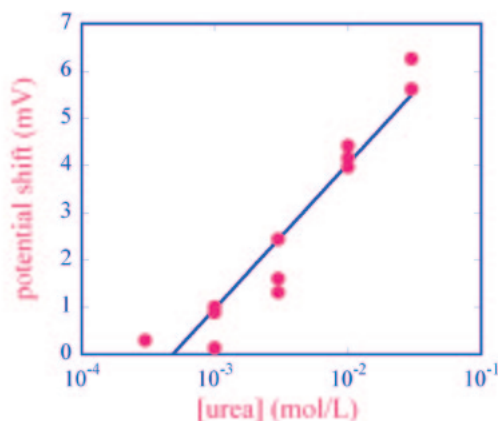

Fig. 18. Potential shift (plotted as a function of the concentration of urea) observed in response to the abrupt change of flow rate from 100 µL/min to 12.5 µL/min.

In this study, a flow channel with an enzyme reaction chamber was fabricated on the sensing surface of LAPS, in which the reaction time was controlled by the flow rate. The variation of the concentration of the substrate was detected in the constant-current mode as a potential shift in the downstream of the chamber.

The cross section of the flow channel in the prototype system was still as large as 1 mm × 1.8 mm, which should be downsized in future for reduction of the solution required for measurement. A differential measurement that detects the variation of the potential before and after the chamber would reduce the drift and lower the detection limit.

Acknowledgements

References

[1] Lundström I, Erlandsson R, Frykman U, Hedborg E, Spetz A, Sundgren H, Welin S, and Winquist F. Artificial 'olfactory' images from a chemical sensor using a light-pulse technique. *Nature* **352**, 47-49, 1991.

[2] Nakao M, Yoshinobu T, and Iwasaki H. Scanning-laser-beam semiconductor pH-imaging sensor. *Sensors and Actuators B* **20**, 119-123, 1994.

[3] Nakao M, Yoshinobu T, and Iwasaki H. Improvement of spatial resolution of a laser-scanning pH-imaging sensor. *Jap J Appl Phys* **33**, L394-L397, 1994.

[4] Inoue S, Yoshinobu T, and Iwasaki H. Chemical imaging sensor using enzyme. *Sensors and Actuators B* **32**, 23-26, 1996.

[5] Uchida H, Zhang WY, and Katsube T. High speed chemical image sensor with digital LAPS system. *Sensors and Actuators B* **34**, 446-449, 1996.

[6] Yoshinobu T, Iwasaki H, Ui Y, Furuichi K, Ermolenko Yu, Mourzina Yu, Wagner T, Näther N, and Schöning MJ. The light-addressable potentiometric sensor for multi-ion sensing and imaging. *Methods* **37**, 94-102, 2005.

[7] Hafeman DG, Wallace Parce J, and McConnel HM, Light-addressable potentiometric sensor for biochemical systems. *Science* **240**, 1182-1185, 1988.

[8] Bergveld P. Development of an ion-sensitive solid-state device for neurophysical measurements. *IEEE Trans Biomed Eng* **BME-17**, 70, 1970.

[9] Matsuo T and Wise KD. An integrated field-effect electrode for biopotential recording. *IEEE Trans Biomed Eng* **BME-21**, 485-487, 1974.

[10] Schöning MJ, Poghossian A, Yoshinobu T, and Lüth H. Semiconductor-based field-effect structures for chemical sensing. *SPIE Proc* **4205**, 188-198, 2001.

[11] Schöning MJ, Abouzar MH, Wagner T, Näther N, Rolka D, Yoshinobu T, Kloock JP, Turek M, Ingebrandt S, and Poghossian A. A semiconductor-based field-effect platform for (bio-)chemical and physical sensors: from capacitive EIS sensors and LAPS over ISFETs to nano-scale devices. In *Mater Res Soc Symp Proc* **952E**, Boston, 0952-F08-02, 2007.

[12] Yoshinobu T, Schöning MJ, Otto R, Furuichi K, Mourzina Y, Ermolenko Y, and Iwasaki H. Portable light-addressable potentiometric sensor (LAPS) for multisensor applications. *Sensors and Actuators B* **95**, 352-356, 2003.

[13] Wagner T, Molina R, Yoshinobu T, Kloock JP, Biselli M, Canzoneri M, Schnitzler T, and Schöning MJ. Handheld multi-channel LAPS device as a transducer platform for possible biological and chemical multi-sensor applications. *Electrochimica Acta* **53**, 305-311, 2007.

[14] Miyamoto K, Sugawara Y, Kanoh S, Yoshinobu T, Wagner T, and Schöning MJ. Image correction method for the chemical imaging sensor. *Sensors and Actuators B* (in press).

[15] Hiroshima Y, Matsumoto S, Kuriyama T, and Kuroda T. CCD image sensors fabricated on epi-wafer. *The IEICE Transactions* **J66-C**, 1004-1011, 1983 (in Japanese).

[16] Nakao M. Visualization of defects in Si wafer using scanning laser-beam chemical microscope. *OYO BUTURI* **69**, 1108−1109, 2000 (in Japanese).

[17] Zhang QT, Wang P, Parak WJ, George M, and Zhang GY. A novel design of multi-light LAPS based on digital compensation of frequency domain. *Sensors and Actuators B* **73**, 152-156, 2001.

[18] Miyamoto K, Kuwabara Y, Kanoh S, Yoshinobu T, Wagner T, and Schöning MJ. Chemical image scanner based on FDM-LAPS. *Sensors and Actuators B* (in press).

[19] Yoshinobu T, Ecken H, Poghossian A, Simonis A, Iwasaki H, Lüth H, and Schöning MJ. Constant-current-mode LAPS (CLAPS) for the detection of penicillin. *Electroanalysis* **13**, 733-736, 2001.